



# Near-unity haze by aluminum induced glass texturing: structural evolution of Al/glass interface and its impact on texturing

MUSTAFA ÜNAL,<sup>1,2,\*</sup> AYDIN TANKUT,<sup>2</sup> SEDAT CANLI,<sup>3</sup> AND RAŞIT TURAN<sup>1,2</sup>

<sup>1</sup>*Micro and Nanotechnology Department, Middle East Technical University, 06800, Ankara, Turkey*

<sup>2</sup>*The Center for Solar Energy Research and Applications, Middle East Technical University, 06800 Ankara, Turkey*

<sup>3</sup>*The Central Laboratory of Middle East Technical University, 06800 Ankara, Turkey*

\*mustafa.unal@metu.edu.tr

**Abstract:** Aluminum induced texturing (AIT) is an effective method to enhance light trapping in thin film solar cells through texturing the surface of the glass substrate. The topography of the textured glass is closely related to the processes that occur at the Al/glass interface during thermal annealing, which is commonly carried out at temperatures above 500 °C. The annealing temperature significantly influences the redox reaction between Al and SiO<sub>2</sub>, and thus the resultant surface texture. In this study, the effect of annealing temperature on the AIT process is investigated in order to elucidate on the evolution of the metallic Al over-layer into the final Al<sub>2</sub>O<sub>3</sub> – c-Si mixture. The structural and compositional changes at the Al/glass interface are compared for samples annealed at varying temperatures. The influence of annealing temperature on the final morphology of the glass surface is also discussed, along with its optical transmittance.

© 2017 Optical Society of America

**OCIS codes:** (240.6648) Surface dynamics; (160.2120) Elements; (160.5140) Photoconductive materials; (240.6700) Surfaces.

## References and links

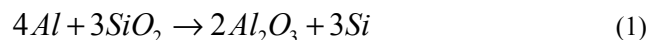
1. J. Son, S. Kundu, L. K. Verma, M. Sakhija, A. J. Danner, C. S. Bhatia, and H. Yang, “A practical superhydrophilic self cleaning and antireflective surface for outdoor photovoltaic applications,” *Sol. Energy Mater. Sol. Cells* **98**, 46–51 (2012).
2. L. K. Verma, M. Sakhija, J. Son, A. J. Danner, H. Yang, H. C. Zeng, and C. S. Bhatia, “Self-cleaning and antireflective packaging glass for solar modules,” *Renew. Energy* **36**(9), 2489–2493 (2011).
3. P. I. Widenborg and A. G. Aberle, “Polycrystalline silicon thin-film solar cells on AIT-textured glass substrates,” *Adv. Optoelectron.* **2007**, 1–7 (2007).
4. J. Hüpkes, S. E. Pust, W. Böttler, A. Gordijn, N. Wyrsch, D. Güttler, A. N. Tiwari, and Y. Gordon, “Light scattering and trapping in different thin film photovoltaic devices,” in: 24th Eur. Photovolt. Sol. Energy Conf.: pp. 2766–2769 (2009).
5. P. Bermel, C. Luo, L. Zeng, L. C. Kimerling, and J. D. Joannopoulos, “Improving thin-film crystalline silicon solar cell efficiencies with photonic crystals,” *Opt. Express* **15**(25), 16986–17000 (2007).
6. X. Yan, S. Venkataraj, and A. G. Aberle, “Modified surface texturing of aluminium-doped zinc oxide (azo) transparent conductive oxides for thin-film silicon solar cells,” *Energy Procedia* **33**, 157–165 (2013).
7. N. Shibata, “Plasma-chemical vapor-deposited silicon oxide / silicon oxynitride double-layer antireflective coating for solar cells,” *Jpn. J. Appl. Phys.* **30**(1), 997–1001 (1991).
8. G. Yang, R. C. M. M. van Swaaij, H. Tan, O. Isabella, and M. Zeman, “Modulated surface textured glass as substrate for high efficiency microcrystalline silicon solar cells,” *Sol. Energy Mater. Sol. Cells* **133**, 156–162 (2015).
9. H. Sannomiya, H. Kumada, M. Murakami, and T. Tomita, Substrate for Solar Cell and Method for Producing the Same, and Thin Film Solar Cell Employing It, WO 2005093854, A1 (1999).
10. W. Zhang, U. W. Paetzold, M. Meier, A. Gordijn, and J. Hüpkes, “Thin-film silicon solar cells on dry etched textured glass,” *Energy Procedia* **44**, 151–159 (2014).
11. D. M. Knotter, “Etching mechanism of vitreous silicon dioxide in HF-based solutions,” *J. Am. Chem. Soc.* **122**(18), 4345–4351 (2000).
12. M. Ünal, H. Nasser, M. Günöven, İ. Sökmen, A. Tankut, and R. Turan, “Effect of aluminum thickness and etching time of aluminum induced texturing process on soda lime glass substrates for thin solar cell applications,” *Phys. Status Solidi* **12**(9-11), 1201–1205 (2015).
13. Y. Huang, F. Law, P. I. Widenborg, and A. G. Aberle, “Crystalline silicon growth in the aluminium-induced

- glass texturing process.” *J. Cryst. Growth* **361**, 121–128 (2012).
- 14. M. Ünal, H. Nasser, M. Günöven, A. Tankut, İ. Sökmen, and R. Turan, “Aluminum induced glass texturing (ait) on soda-lime, borosilicate, alkali-free and fused silica glass for thin film solar cell applications,” in: 31st Eur. Photovolt. Sol. Energy Conf. Exhib.: pp. 230–234 (2015).
  - 15. O. Isabella, J. Krc, and M. Zeman, “Modulated surface textures for enhanced light trapping in thin-film silicon solar cells,” *Appl. Phys. Lett.* **97**(10), 101106 (2010).
  - 16. P.I. Widenborg, S. V. Chan, T. Walsh, A. G. Aberle, “Thin-film poly-Si solar cells on AIT-textured glass - Importance of the rear reflector,” *Conf. Rec. IEEE Photovolt. Spec. Conf.* 7–9 (2008).
  - 17. N. Sahraei, S. Venkataraj, A. G. Aberle, and M. Peters, “Optimum feature size of randomly textured glass substrates for maximum scattering inside thin-film silicon solar cells,” *SPIE Photonics West 2014-OPTO Optoelectron. Devices Mater.* **8981**, 89811D (2014).
  - 18. M. Lluscà, J. D. Santos, S. Fernández, J. P. González, J. J. Gandia, J. Cárate, A. Antony, J. M. Asensi, and J. Bertomeu, “Textured Glass Substrates for Thin Film Silicon Solar Cells,” in: 28th Eur. Photovolt. Sol. Energy Conf. Exhib.: pp. 2170–2174 (2012).
  - 19. N. Chuansuwanich, P. Campbell, P. I. Widenborg, A. Straub, and A. G. Aberle, “Light trapping properties of evaporated poly-silicon films on AIT-textured glass substrates,” *Conf. Rec. Thirty-First IEEE Photovolt. Spec. Conf.* 2005, 1161–1164 (2005).
  - 20. A.G. Aberle, P.I. Widenborg, N. Chuansuwanich, *Glass Texturing*, EP1613562, 2004.
  - 21. H. A. Wriedt, “The Al-O (Aluminum-Oxygen) System,” *Bull. Alloy Phase Diagrams*. **6**(6), 548–553 (1985).
  - 22. H. Hirata and K. Hoshikawa, “Oxygen solubility and its temperature dependence in a silicon melt in equilibrium with solid silica,” *J. Cryst. Growth* **106**(4), 657–664 (1990).
  - 23. M. Stöger-Pollach, T. Walter, M. Muske, S. Gall, and P. Schattschneider, “Phase transformations of an alumina membrane and its influence on silicon nucleation during the aluminium induced layer exchange,” *Thin Solid Films* **515**(7–8), 3740–3744 (2007).
  - 24. J. Schneider, A. Sarikov, J. Klein, M. Muske, I. Sieber, T. Quinn, and H. S. Reehal, “A simple model explaining the preferential (1 0 0) orientation of silicon thin films made by aluminum-induced layer exchange,” *J. Cryst. Growth* **287**, 423–427 (2006).
  - 25. J. Schneider, A. Schneider, A. Sarikov, J. Klein, M. Muske, S. Gall, and W. Fuhs, “Aluminum-induced crystallization: Nucleation and growth process,” *J. Non-Cryst. Solids* **352**(9–20), 972–975 (2006).
  - 26. J. Klein, J. Schneider, M. Muske, S. Gall, and W. Fuhs, “Aluminium-induced crystallisation of amorphous silicon : influence of the aluminium layer on the process,” *Thin Solid Films* **452**, 481–484 (2004).
  - 27. J. Schneider, J. Klein, M. Muske, S. Gall, and W. Fuhs, “Aluminum-induced crystallization of amorphous silicon : preparation effect on growth kinetics,” *J. Non-Cryst. Solids* **340**, 127–130 (2004).
  - 28. O. Nast, S. Brehme, S. Pritchard, A. G. Aberle, and S. R. Wenham, “Aluminium-induced crystallisation of silicon on glass for thin-film solar cells,” *Sol. Energy Mater. Sol. Cells* **65**, 385–392 (2001).
  - 29. S. Gall, M. Muske, I. Sieber, O. Nast, and W. Fuhs, “Aluminum-induced crystallization of amorphous silicon,” *J. Non-Cryst. Solids* **302**, 741–745 (2002).
  - 30. A. Mohiddon and G. Krishna, “Metal Induced Crystallization,” in *Crystallization – Science and Technology*, Marcello Rubens Barsi Andreatta, ed. (Intech, 2012), pp. 461–480.
  - 31. W. Cui, C. Wang, J. Yan, Z. Wang, and D. Wei, “Ultrasonics Sonochemistry Wetting and reaction promoted by ultrasound between sapphire and liquid Al – 12Si alloy,” *Ultrason. - Sonochemistry*. **20**(1), 196–201 (2013).
  - 32. T. Huang, N. Chen, X. Zhang, Y. Bai, Z. Yin, H. Shi, H. Zhang, Y. Wang, Y. Wang, and X. Yang, “Aluminum induced crystallization of strongly (111) oriented polycrystalline silicon thin film and nucleation analysis,” *Sci. China Technol. Sci.* **53**(11), 3002–3005 (2010).
  - 33. J. L. Murray and A. J. McAlister, “The Al-Si (Aluminum-Silicon) System,” *Bull. Alloy Phase Diagrams*. **5**(1), 74–84 (1984).
  - 34. S. C. Flood and J. D. Hunt, “Modification of Al-Si eutectic alloys with Na,” *Met. Sci.* **15**(7), 287–294 (1981).
  - 35. S. Shankar, Y. W. Riddle, and M. M. Makhoul, “Nucleation mechanism of the eutectic phases in aluminum-silicon hypoeutectic alloys,” *Acta Mater.* **52**(15), 4447–4460 (2004).
  - 36. S. Hegde and K. N. Prabhu, “Modification of eutectic silicon in Al-Si alloys,” *J. Mater. Sci.* **43**(9), 3009–3027 (2008).
  - 37. A. K. Dahle, K. Nogita, S. D. McDonald, C. Dinnis, and L. Lu, “Eutectic modification and microstructure development in Al-Si Alloys,” *Mater. Sci. Eng. A* **413–414**, 243–248 (2005).
  - 38. W. Burger and M. J. Burge, “The Discrete Fourier Transform in 2D,” in: *Digital Image Processing: An Algorithmic Introduction Using Java*, 1st ed. (Springer, 2008), pp. 343–366.

## 1. Introduction

The ability to control the surface texturing of glass offers several advantages in enhancing the light trapping for various solar cell technologies including conventional Si wafer solar modules (texturing the packaging glass [1,2]) as well as various thin film approaches (texturing the substrate/superstrate [3,4]). Light trapping is especially important for thin film solar cells, where minimal absorber material usage (i.e., thickness) is necessary to achieve cost-competitiveness. Thin film solar cells are often produced by growing functional layers

(contacts, absorber, buffer layer, ARC, etc.) sequentially onto glass [5–7]. Therefore, texturing of the glass surface prior to the deposition of the solar cell components promises a low cost and effective method for increasing the efficiency of capturing light. Modifying the glass surface can help increase the fraction of diffused light inside the absorber layer, resulting in an increase in the optical path length [8]. Since the texturing is achieved at the beginning of the process flow, it does not add any complication (thermal load, chemical contamination, etc.) to the subsequent steps. Several techniques for glass texturing have been proposed, such as sandblasting [9], dry etching [10], wet etching [11] and aluminum induced texturing (AIT) [12]. Among these, AIT is of particular interest due to its minimal damage on the bulk of the glass and precise texture control [12]. In AIT, a thin aluminum film is used as a sacrificial layer to produce nano- and micro-sized craters on the surface of glass [12,13]. The process is chiefly governed by the random redox reaction between Al and SiO<sub>2</sub> as shown below [14].



The redox reaction is induced by annealing the Al-coated glass at temperatures above 500 °C. Annealing temperature 500 and 620 °C have been reported [3,15–20]. According to Huang et. al. [13], at the beginning of the annealing process, Al<sub>2</sub>O<sub>3</sub> nodules are formed and grow inside of the glass, while Si dissolves into the surrounding Al and forms Si clusters. After annealing process, the reaction products are chemically etched, leaving behind a bare, textured glass surface. Since the final surface morphology of glass is directly influenced by the redox reaction, a better understanding of the thermodynamic processes that occur during annealing would lead to improved control of the optical properties of glass. One such attempt is presented in this study, which investigates the effect of annealing temperature on the Al/glass interface and the final surface texture. As discussed below, two separate mechanisms through which the redox reaction occurs are observed, depending on the annealing temperature.

## 2. Experimental

AIT experiments were carried out on 10 mm x 10 mm clear soda-lime float glass (Türkiye Şişe ve Cam Fabrikaları A.Ş) with a thickness of 4 mm for annealing experiments. Softening point of the glass is 727 °C. Prior to Al coating, all samples were cleaned by a chemical detergent in ultrasonic bath at 50 °C followed by DI rinse. Following the surface cleaning, 150nm of Al was deposited via thermal evaporation at a base pressure of  $3 \times 10^{-5}$  torr and an average deposition rate of 2 nm/sec. For optical measurements, the glass was cut into 30 mm x 30 mm samples.

Annealing runs were carried out in a classical tube furnace (10 cm diameter) under 4 slm N<sub>2</sub> flow (preliminary annealing experiments under air revealed the formation of micron-scale, blister-like features, which diminished the effectiveness of texturing). As listed in Table 1, samples were labelled according to their respective annealing temperature (in °C) and duration (in min.), such that sample 550\_105 was annealed at 550 °C for 105 min. Following the annealing step, the samples were etched for 1 hour using a NaOH:H<sub>2</sub>O<sub>2</sub>:H<sub>2</sub>O mixture with a ratio of 1:2:6. A bare glass and an Al coated glass sample (no annealing) were prepared as reference for the optical measurements, and were labelled as Ref1 and Ref2, respectively (the Al layer on Ref2 was removed via the identical chemical etching method as the rest of the sample set).

**Table 1.** List of samples used in the AIT experiments. The number before the underscore designates the annealing temperature in °C, and the one after denotes the annealing duration in minutes

550 °C			575 °C		600 °C		
550_005	550_015	550_060	575_015	575_030	600_005	600_010	600_011
550_090	550_105	550_120	575_045	575_060	600_012	600_013	600_020
550_150	550_180	550_300	575_075	575_090	600_030	600_040	600_050
550_600	550_1020		575_105		600_060		

Structural, morphological, and optical characterization of the samples were made before and after etching. The morphology and the elemental distribution of the annealed film was investigated by an optical microscope (Nade metallurgical microscope - NMM-800TRF) and a QUANTA 400F field emission scanning electron microscope (FE-SEM) coupled with an Ametek EDAX energy dispersive X-ray spectroscope (EDX). The structural and compositional evolution of the over-layer was studied by Raman spectroscope (Horiba 800 Jobin Yvon). Selected EDX images were processed using Adobe Photoshop CC 2015. After texturing of samples, optical measurements were conducted with an 8-inch, 5-port integrating sphere (Oriel 70679NS), angle resolved scattering system and topographical characterization with SEM (Zeiss EVO HD) and atomic force microscope (Veeco diMultiMode V) using a ATEC-NC-20 tip in tapping mode. 2D FFT images were obtained from AFM data using image analyses software Gwyddion version 2.44.

### 3. Results

#### 3.1 Annealing experiments

The optical micrographs (OM) and corresponding Raman spectra obtained from samples annealed at 550 °C for 90 and 120 min (550\_090 and 550\_120, respectively) are given in Fig. 1(a) through Fig. 1(f). The OM of the 550\_090 sample shows a high contrast Al background darker, micrometer sized spots dispersed on the surface. In addition, agglomerate-like features with low contrast can be observed, as seen in the center of the higher magnification image given in Fig. 1(b) (taken by the built-in optical microscope of the Raman spectroscope). The laser beam of the tool was focused on the agglomerate-like feature, and Raman spectra was obtained [Fig. 1(c)]. The Raman peak near 521 cm<sup>-1</sup> is distinguishable, which corresponds to crystalline Si. Accordingly, it appears that nucleation of the reduced Si has already begun at 90 min, and the dark features are Si precipitates. The optical images for the 550\_120 sample [Fig. 1(d) and Fig. 1(e)] show that the precipitates further grow into dendritic structures with a distinct crystalline Si Raman peak, as shown in Fig. 1(f). To investigate on the compositional distribution of the annealed samples, EDX mapping was carried out for silicon, oxygen and aluminum.

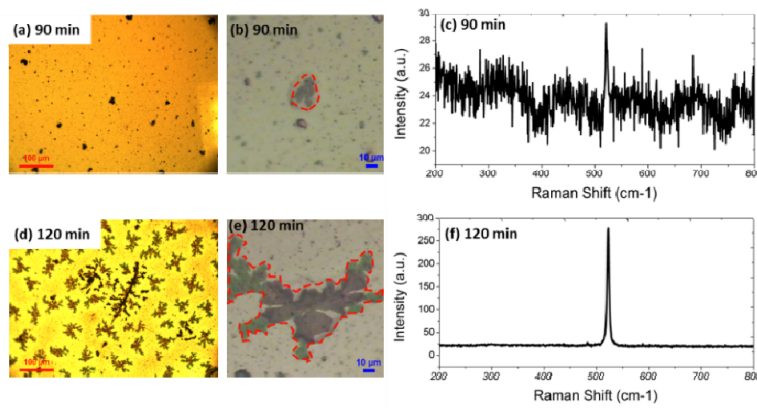


Fig. 1. (a) OM of 550\_090, (b) image from built-in optical microscope of Raman spectrometer of 550\_090, (c) Raman spectra of 550\_090, (d) OM of 550\_120, (e) image from built-in optical microscope of Raman spectrometer of 550\_120, (f) Raman spectra of 550\_120.

Figure 2(a) and Fig. 2(b) shows EDX maps taken from samples 550\_120 and 550\_300, along with their respective secondary electron (SE) images. The brightness of the color is proportional to the signal intensity obtained from its respective element. A distinct compositional separation is noticeable on the 550\_120 sample, where the dendritic Si islands are enclosed by a mixture of Al and O [Fig. 2(a)]. In the near-vicinity of the Si dendrites Al signal is particularly bright, whereas the O map reveals very low contrast. The high contrast Al regions are considered to be metallic Al, while the surrounding area is aluminum oxide. In Fig. 2(b), EDX map of Si, O and Al for 550\_300 is given with corresponding SEM image. In this sample, Si dendrites appear to have grown into a more equiaxed morphology and no metallic Al is present near them.

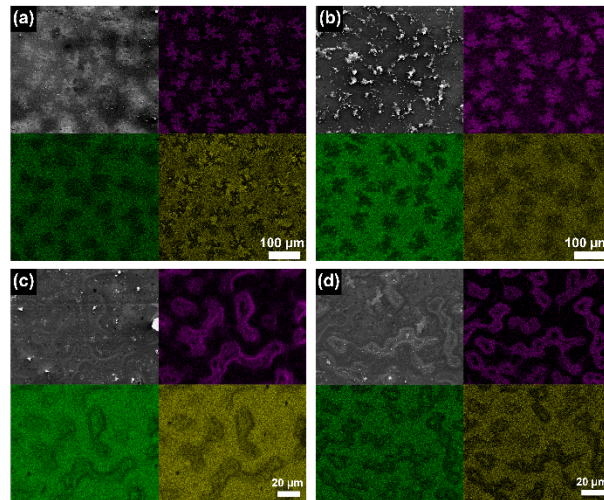


Fig. 2. EDX mapping for (a) 550\_120, (b) 550\_300, (c) 575\_105 and (d) 600\_060. Secondary electron image (top left) and maps of Si (top right), O (bottom left) and Al (bottom right).

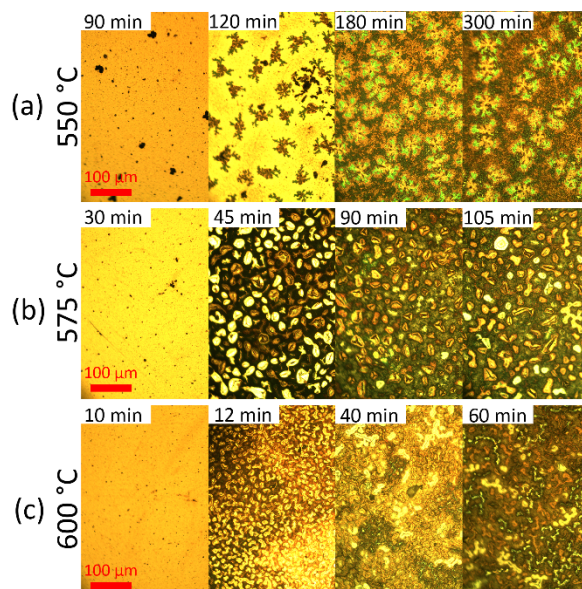


Fig. 3. Optical images of annealed samples with varying durations at a temperature of a) 550 °C, b) 575 °C, c) 600 °C. All images are obtained using reflected light.

The evolution of the surface morphology during 550 °C annealing can be monitored by the optical micrographs taken from samples annealed for varying times, as shown in Fig. 3(a). The dendritic Si crystals reach their final structure between 120 and 180 min. of annealing, and further annealing up to 300 min. does not produce a significant effect. For the 550\_120 sample, the dendritic structures yield low contrast, while for longer annealing times, they appear bright and the surrounding area have a brownish color. This discrepancy is likely due to the reduction in the amount of reflected light from the oxidized Al background, which results in the change in the relative contrast between the dendrites and the background. When the micrographs of the 550 °C annealed samples are compared to those of 575 °C [Fig. 3(b)] and 600 °C [Fig. 3(c)], a drastic difference in the morphology of the surface feature can be seen. At 575 °C and 600 °C annealing, circular features are visible instead of Si dendrites at the early stages of annealing. Upon further annealing, these structures coalesce into unidirectional, “peanut-shell” shaped features (we will refer to these features as “peanuts” for the rest of the text). These features appear smaller for the samples annealed at 600 °C compared to those annealed at 575 °C. Figure 3 also shows that the necessary annealing time to complete the reaction reduced significantly with increasing annealing temperature.

Figure 2(c) and Fig. 2(d) lists the SE images and EDX maps (Si, O, Al) for samples annealed at 575 and 600 °C, respectively. The annealing durations were chosen to ensure that the process reached completion (i.e., all of the Al has been oxidized) for each sample. It is noticeable that the peanut-like structures formed at 575 and 600 °C are not compositionally uniform; Si-rich regions are located at the periphery, and a high concentration of Al and O is detectable inside of these features. The separation is particularly distinguishable for the sample annealed at 600 °C [Fig. 2(d)].

### 3.2 Etched glass surfaces

Following the annealing runs, the samples were chemically etched by an alkaline solution to remove the reactions products, and the texture of the bare glass samples were investigated via SEM. Figure 4 shows micrographs with varying magnification and viewing angles, taken from samples representing different stages of annealing at 550 °C. At 90 min. depressions (“craters”) up to 2 μm diameter are distributed on the flat glass surface [Fig. 4(a)]. After

120 min. of annealing, the crater density have increased significantly, while flat areas can still be detected, as shown in Fig. 4(b). The craters coalesced into larger groups, forming a foam-like network on the surface. At the end of 300 min. [Fig. 4(c)] the surface is completely textured. The flat zones observed for sample 550\_120 appear to be textured in 550\_300, albeit with a smaller crater size compared to their surroundings.

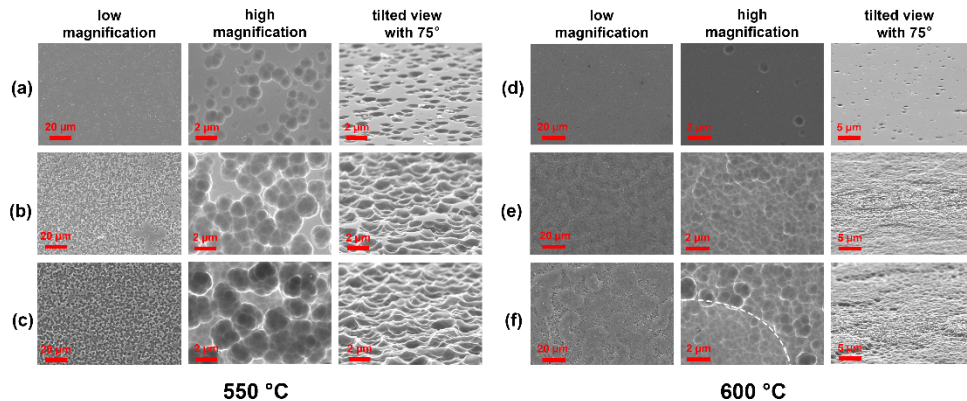


Fig. 4. SEM images of samples after etching. (a) 550\_090, (b) 550\_120, (c) 550\_300, (d) 600\_010, (e) 600\_030, and (f) 600\_060. Left column shows low magnification image, middle high magnification image, and right tilted view for each temperature.

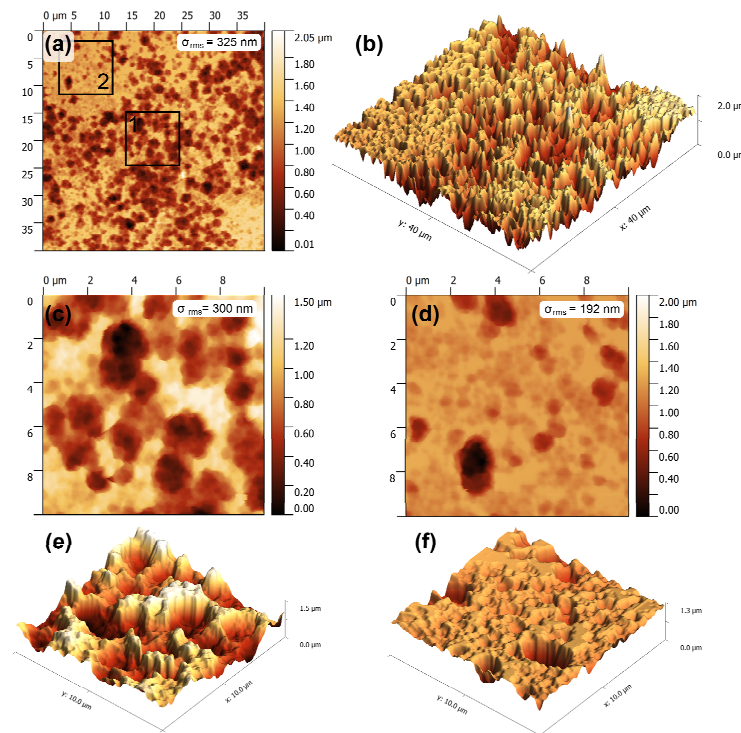


Fig. 5. AFM images of sample 550\_300. (a) 2D image with 40  $\mu\text{m}$  x 40  $\mu\text{m}$  scan area (b) 3D image with 40  $\mu\text{m}$  x 40  $\mu\text{m}$  scan area, (c) 2D image with 10  $\mu\text{m}$  x 10  $\mu\text{m}$  scan area of the place indicated as “1” in the image with 40  $\mu\text{m}^2$  scan area (d) 2D image with 10  $\mu\text{m}$  x 10  $\mu\text{m}$  scan area of the place indicated as “2” in the image with 40  $\mu\text{m}^2$  scan area, (e) 3D image of “1” with 10  $\mu\text{m}$  x 10  $\mu\text{m}$  scan area and (f) 3D image of “2” with 10  $\mu\text{m}$  x 10  $\mu\text{m}$  scan area.

The bare glass surfaces from the samples annealed at 575 °C and 600 °C were quite similar to each other, therefore, only the SEM images of the latter is presented. Figure 4(d) shows secondary electron micrographs obtained from the sample annealed at 600 °C for 10 min. Craters with a diameter of 1 μm or less can be seen randomly distributed on the glass surface. At 30 min of annealing, the surface is fully covered with craters, a pattern can be seen due to the contrast difference in the plan view images [Fig. 4(e)]. The pattern resembles the peanut-like shapes shown Fig. 2(d). The 75° tilted view reveals that the observed contrast in the plan view images is due to a height difference between adjacent regions. After 60 min. of annealing, the peanut-like features appear larger, and the height difference is more pronounced [Fig. 4(f)]. It can also be noted that the craters on these features appear to be smaller than those on the surrounding areas.

Figure 5 shows 2D and 3D AFM images of 550\_300 with 40 μm x 40 μm and 10 μm x 10 μm scan areas. The surface roughness ( $\sigma_{rms}$ ) for measurement with 40 μm<sup>2</sup> scan area is 325 nm [Fig. 5(a)]. In both 2D and 3D AFM image of 550\_300, Fig. 5(a) and Fig. 5(b), there are relatively flat areas on the surface. Highly textured area is numbered with “1” while relatively flat area numbered with “2”. When 10 μm x 10 μm images taken from these two areas are compared it can be seen that in area “1” there are deep craters (with diameter approximately 2 μm) and the surface roughness is 300 nm as given in Fig. 5(c). On the other hand, in the area “2” at Fig. 5(d), there are a few deep craters which are predominantly made up of shallow craters with the surface roughness, 192 nm as given in Fig. 5(d). The difference between these two areas can be seen clearly in 3D AFM images given in Fig. 5(e) and Fig. 5(f).

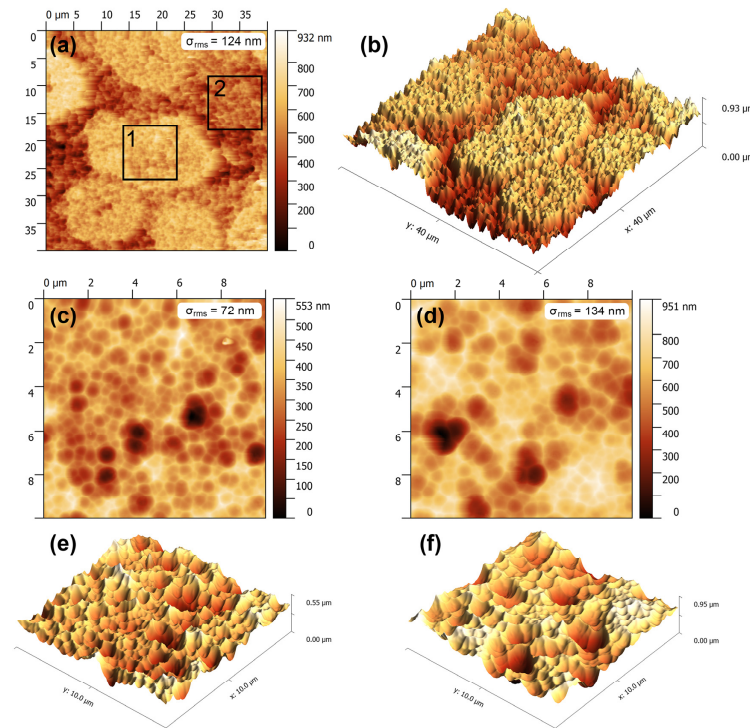


Fig. 6. AFM images of 600\_060. (a) 2D image with 40 μm x 40 μm scan area (b) 3D image with 40 μm x 40 μm scan area, (c) 2D image with 10 μm x 10 μm scan area of the place indicated as “1” in the image with 40 μm<sup>2</sup> scan area (d) 2D image with 10 μm x 10 μm scan area of the place indicated as “2” in the image with 40 μm<sup>2</sup> scan area, (e) 3D image of “1” with 10 μm x 10 μm scan area and (f) 3D image of “2” with 10 μm x 10 μm scan area.

On the other hand, in Fig. 6, 2D and 3D AFM images of 600\_060 with  $40 \mu\text{m} \times 40 \mu\text{m}$  and  $10 \mu\text{m} \times 10 \mu\text{m}$  scan areas are given. The surface roughness ( $\sigma_{\text{rms}}$ ) for measurement with  $40 \mu\text{m}^2$  scan area [Fig. 6(a)] is 124 nm. The peanut-like features observed by other imaging techniques above can also be seen in the wide area scans [Fig. 6(a) and Fig. 6(b)]. These areas are elevated from the surface by approximately 500 nm. When the surface of this elevated area is investigated [Fig. 6(c)], it is seen that the surface craters have diameter smaller than 500 nm resulting in a local roughness of 72 nm. However, on the surrounding area [Fig. 6(d)], the craters are larger ( $>700 \text{ nm}$ ) and the surface roughness is considerably higher (134 nm). The difference between two surface can be compared in Fig. 6(e) and Fig. 6(f) with 3D images.

### 3.3 Optical measurements

To compare the optical properties of the textured samples annealed at different temperatures, total transmittance and haze (ratio of the diffused transmittance to total transmittance) measurements were carried out. The light was sent through the textured side and the integrated sphere was placed behind, facing the flat side of the sample. All samples were “fully annealed”, i.e., further annealing did not produce a change in the surface morphology (since temperature uniformities were observed for the 30 mm x 30 mm sample annealed at 550°C, the annealing duration was chosen as 600 min to ensure the process was completed across the sample surface). The % transmittance values distributed between wavelengths of 350 nm and 1100 nm were similar for all AIT samples as well as samples Ref1 and Ref2, as shown in Fig. 7(a). Transmittance of the 550\_600 sample appeared several percentage points (pp) higher than the rest of the samples. The haze values from representative AIT and reference samples are given in Fig. 7(b). As expected, diffused transmittance for the non-textured Ref1 and Ref2 is negligible, while considerable haze was observed for the AIT samples at all wavelengths measured. Among these, the 550\_600 sample showed significantly more haze than its 575 and 600 °C counterparts (between 20 to 40 pp, depending on the wavelength of the incoming light).

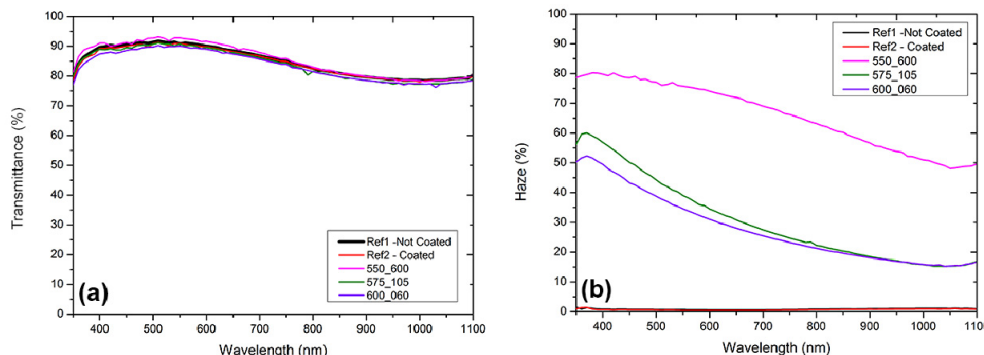


Fig. 7. (a) Transmittance and (b) haze of samples annealed at different temperatures and durations with 2 reference sample.

## 4. Discussion

### 4.1 Structural and chemical evolution of the over-layer

The observations from the annealing experiments at different temperatures are presented in the above section. Several commonalities exist amongst all temperatures examined. At the onset of annealing, micron-scale Al<sub>2</sub>O<sub>3</sub> nodules are distributed on the surface (Fig. 3, leftmost column), which, after chemical etching, manifest themselves as craters with several  $\mu\text{m}$  diameters (Fig. 4, top row). As the annealing continues, distinct features appear on the surface, consisting (at least partially) of crystalline Si [Fig. 1(a) through Fig. 1(f)]. The

process continues until no available metallic Al is present at the glass surface. These observations are well in accord with the AIT model presented by Huang et. al. [13].

However, the morphology of the Si-rich regions show considerable variation based on annealing temperature, and indicates a fundamental difference in the crystallization of Si. Whereas the Si crystals grow into a distinctly dendritic shape at 550 °C [Fig. 2(a)], they form as a layer around the edges of Al-oxide structures at and above 575 °C [Fig. 2(c) and Fig. 2(d)]. In an attempt to explain this apparent discrepancy, we make two assumptions to simplify the materials system:

- (1) Glass is assumed to be composed solely of  $\text{SiO}_2$ , while the effect of other components (alkali oxides, etc.) is ignored.
- (2) We consider  $\text{SiO}_2$  and  $\text{Al}_2\text{O}_3$  to be chemically inert and neglect the effect of oxygen (considering the minute solubility of O in Al and Si at the temperatures of concern [21,22]).

The problem can then be reduced to an isothermal Al-Si system where the composition of Si with respect to Al is increasing with time (as the redox reaction progresses). As such, we can refer to the Al-Si phase diagram (Fig. 8) and discuss the possible crystallization mechanisms for the low temperature (550 °C) and high temperature (600 °C) processes separately.

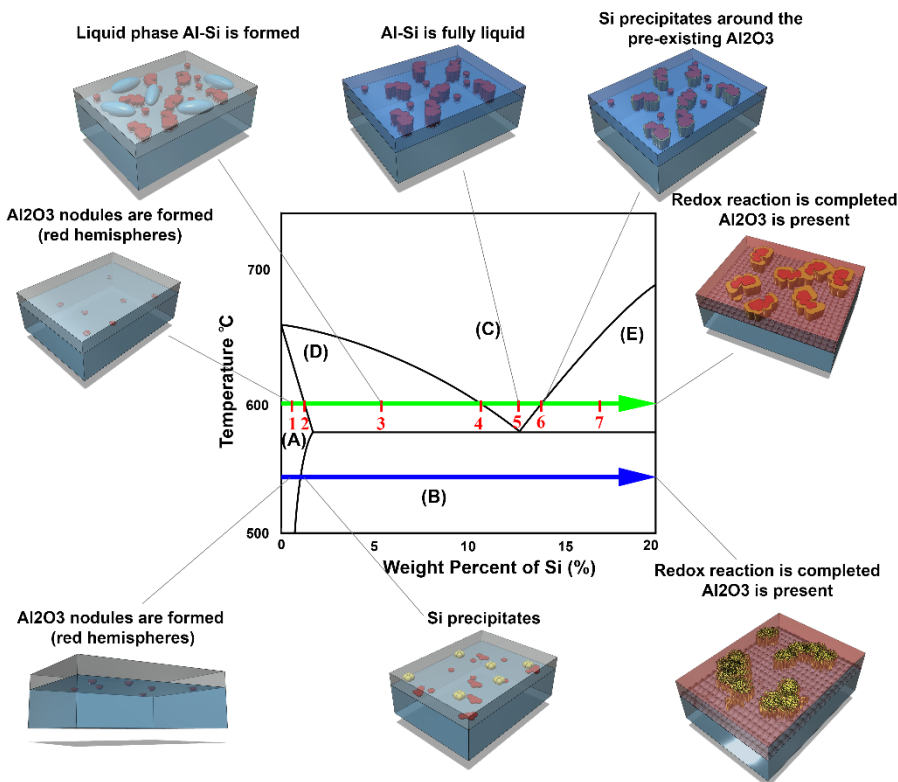


Fig. 8. Al-Si phase diagram with sketches illustrating the evolution of the film and interface morphology. Phase regions are defined as (A)  $\alpha$ -Al (<1.3% Si), (B)  $\alpha$ -Al + Si, (C) Liquid Al (~11-14% Si), (D)  $\alpha$ -Al (<1.3% Si) + Liquid Al (~11% Si) and (E) Liquid Al (~14% Si) + Si (~100% Si).

At the beginning of annealing the system consists solely of Al. As the reaction ensues, the chemically reduced Si dissolves in Al and its composition w.r.t. Al increases rapidly, as indicated by the blue (550 °C) and green (600 °C) arrows in Fig. 8. At 550 °C, as the

concentration of Si exceeds the solubility limit (approximately 1.1%) nucleation occurs, forming Si crystallites within the solid Al matrix. The location of the available Al is dictated by the network of  $\text{Al}_2\text{O}_3$  particles at this stage. At this stage, the process resembles the nucleation and growth mechanisms observed for Al induced crystallization, where the Al-grain boundaries and Al-oxide surface act as preferential nucleation sites for Si [23–29]. Originally closer to a circular shape [Fig. 1(a) and Fig. 1(b)], the crystallites respond to local fluctuations of Si concentration in the surrounding Al and grow into a dendritic form [30] [Fig. 1(d) and Fig. 1(e)]. As the  $\text{Al}_2\text{O}_3$  growth compete with that of the Si dendrites for lateral space, the expansion of the latter is restricted within the available Al. This can easily be seen by comparing Fig. 9(a) and Fig. 9(b), where the EDX maps presented in Fig. 2(a) and Fig. 2(b) are overlaid to show the composition near the Si dendrites for samples annealed at 550 °C for 120 and 300 min., respectively. At 120 min. regions rich in Al (i.e., poor in oxygen) are visible, particularly in between the “branches” of the Si-dendrites, while the background is predominantly of  $\text{Al}_2\text{O}_3$  [Fig. 9(a)]. As the growth is confined into the Al, the Si crystals become more compact in shape, while the effective radii (approximately 50  $\mu\text{m}$ ) does not change appreciably at 300 min. of annealing [Fig. 9(b)]. Our explanation of the processes that occur at 550 °C is based on the work published by Huang et. al., which investigated the AIT process at 570 °C and observed the formation of dendritic Si [13], very similar to those shown in the present study.

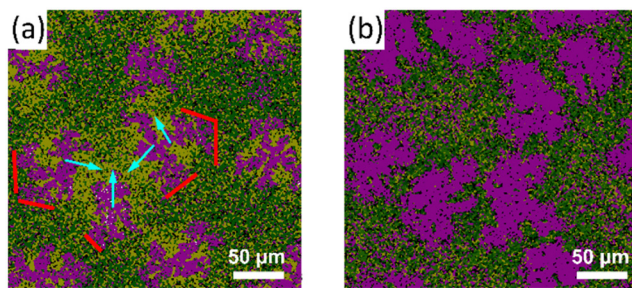


Fig. 9. Overlaid Si, Al, and O EDX maps of (a) 550\_120 and (b) 550\_300. The green arrows indicate the direction that Si dendrites are allowed to grow, while the red lines suggest where growth is restricted.

The annealing process at 600 °C commences similarly to that at 550 °C: The Si produced in the redox reaction is dissolved in Al (“#1”, as labelled in Fig. 8), forming a solid solution, until the concentration of Si in Al exceeds the solubility limit (#2, approximately 1.3%). Beyond this point (#3), addition of Si into the system results in the formation of a liquid Al-Si phase (with a Si concentration of approximately 11.0%) within the saturated Al solid phase (Si concentration of approximately 1.3%). The fraction of the liquid phase increases as Si is introduced (and Al is removed) until the system is fully liquid at an overall Si concentration of 11.0% (#4). The system stays as a single liquid phase (#5), until the Si concentration reaches ~14.0% (#6), after which the nucleation of Si is initiated (#7). The Si precipitates continue to grow until there is no available Al left to sustain the redox reaction at the glass surface. Using this model, we can then explain the structural formation of crystal Si as follows: At #2, Si saturated Al phase is present, wherein  $\text{Al}_2\text{O}_3$  particles are dispersed randomly. Upon the formation of the liquid phase, the rate of redox reaction at the liquid/glass interface increases drastically due to enhanced transport mechanism. This results in a positive feedback loop where the increase in the amount of liquid phase increases the production of Si, and vice versa. This cascading reaction kinetics is apparent in OM images presented in Fig. 10, where a sudden change in morphology between 11 minutes and 12 minutes of annealing can be seen. The Si concentration rapidly reaches past #6, and precipitation begins. The  $\text{Al}_2\text{O}_3$  surface acts as a highly preferential nucleation site for Si, which wraps around the  $\text{Al}_2\text{O}_3$  regions to form the structures seen in Fig. 2(b). A similar

phenomenon where Si segregation on  $\text{Al}_2\text{O}_3$  was observed for the cooling of eutectic Al-Si mixture in a previous study [31].

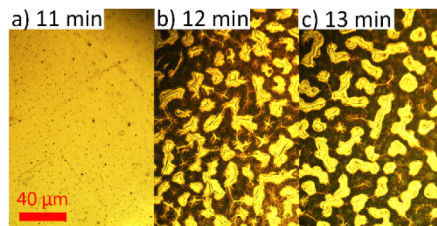


Fig. 10. Optical microscope images of (a) 600\_011, (b) 600\_012 and (c) 600\_013.

#### 4.2 Texturing mechanism and the effect of annealing temperature

As understood from the present study as well as those carried out previously [13], the fundamental texturing mechanism of AIT formation of  $\text{Al}_2\text{O}_3$  particles and their expansion into the glass, which manifest themselves as micro-craters on the glass surface after chemical etching of the over-layer. On the other hand, the simultaneous production of elemental Si results in processes that affect the crater formation depending on the temperature at which the annealing is carried out.

As the precipitates grow, they act as a diffusion barrier between Al and glass, hindering the redox reaction. This is apparent in Fig. 11(a) and Fig. 11(b), where the Si-EDX map from the Al over-layer of the 550\_120 sample (prior to chemical etching) is compared to the SE micrograph of the same sample after etching as well as in AFM images in Fig. 5. Relatively flat regions with shapes that resemble the Si dendrites are clearly visible on the etched glass. The lateral size of the flat zones appear to be smaller compared that of the Si dendrites, possibly indicating that the growth of Si extends onto the  $\text{Al}_2\text{O}_3$  particles during the later stages of annealing.

A more complex phenomenon is observed at 600 °C, which is well above the Al-Si eutectic temperature, 577 °C [32–36]. The increase in the Si concentration in Al promotes the formation of a liquid phase. Where the liquid phase is in contact with the glass, the rate of the redox reaction is significantly enhanced, therefore, a more rigorous etching pattern is expected. In Fig. 11(c) and Fig. 11(d), it is seen that the shape of peanut-like structures seen during annealing are imprinted on the glass surface as distinct regions following the chemical etching of the over-layer. These regions have a lower crater-size distribution and appear to be elevated by 500 nm compared to their surroundings [Fig. 4(f), Fig. 6(a) and Fig. 6(b)]. The peanut-like structures were formed during the initial phase of annealing, while the Al was solid, and were subsequently enclosed by Si upon its precipitation. As such, the glass under these regions were kept from interacting with liquid Al, thus have a lighter etch pattern.

It is worthwhile to mention that the AIT experiments carried out at 575 °C and 600 °C appear very similar, indicating the formation of a liquid Al-Si phase in both cases. Considering that the eutectic temperature of the pure Al-Si system is 577 °C, texturing at 575 °C would be expected to occur in solid phase only, similar to 550 °C. This is likely an indication that the additional elements introduced through the glass (Na, Mg etc.) resulted in a decrease in the eutectic temperature of the system, as suggested by previous studies that reveal such a modification of the Al-Si system [34,36,37].

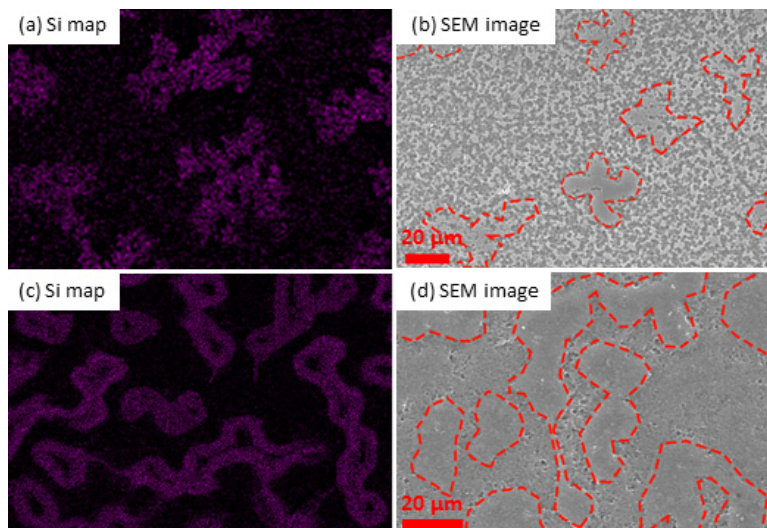


Fig. 11. Comparison of EDX map of Si with textured surface. (a) EDX map of Si belongs to 550\_120, (b) SEM image of 550\_120 after etching. (c) EDX map of Si belongs to 600\_060 and (d) SEM image of 600\_060 after etching process. Plateaus are circled with red dashes.

#### 4.3 Optical measurements

Optical measurements given in Fig. 7(a) and Fig. 7 (b) show that the diffused transmittance in sample annealed at 550 °C is greatly enhanced compared to its counterparts annealed at higher temperatures. The haze is approximately 20 pp higher at low wavelengths (near 400 nm) for the former, and the difference reaches up to 40 pp at higher wavelengths (near 1100 nm). This significant difference in haze can be correlated to the difference in surface texture of samples annealed only in solid phase (i.e., at 550 °C) and those experienced the formation of a liquid phase (at 575 and 600 °C). As explained in the previous section the overall surface texture is relatively uniform for samples annealed at 550 °C, whereas two distinct regions with different texture characteristics are observed at higher annealing temperatures (depending on whether the redox reaction between Al and SiO<sub>2</sub> occurred at the solid/solid or the liquid/solid interface). In order to elucidate the texture periodicity of samples annealed at different temperatures, 2D Fast Fourier Transform (2D FFT) images are created using representative AFM images of samples annealed at 550 and 600 °C, as shown in Fig. 12. For both cases, the highest intensity is seen at the center of the map, which corresponds to scattering events associated with lowest spatial frequencies, thus transmission is almost entirely specular. The scattering events with higher frequencies (i.e., diffused scattering) are represented with a higher k-vector, thus are further away from the center [38]. It can easily be seen that as at higher k-vectors the brightness of the sample 550\_300 is significantly greater to that of the sample 600\_060, suggesting a higher haze value over a wide range of frequencies.

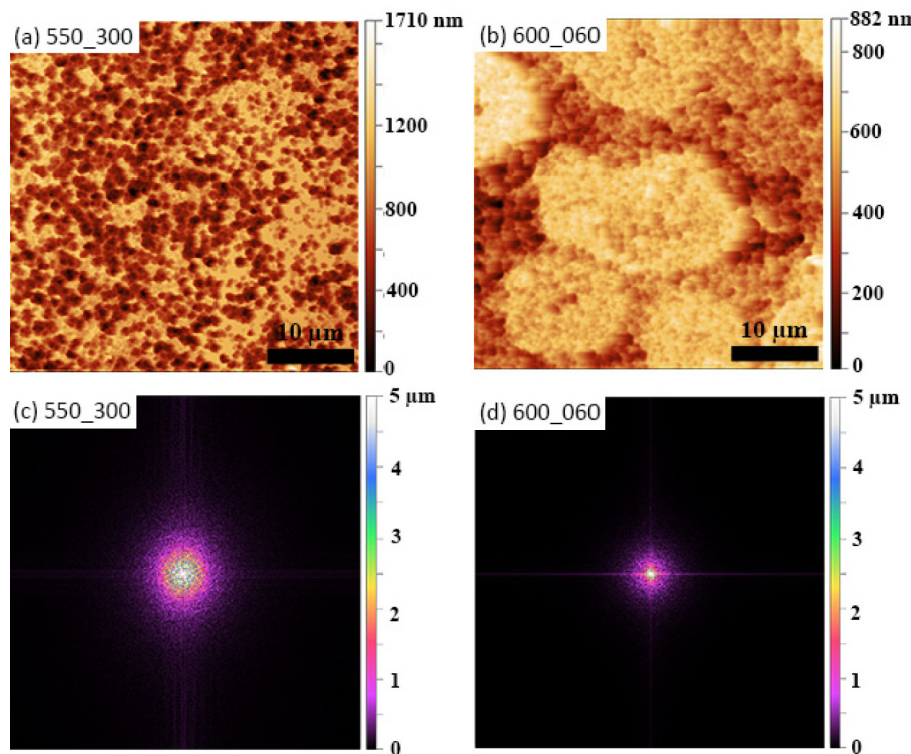


Fig. 12. Comparison of surfaces by Fast Fourier Transform (FFT) of  $40 \mu\text{m} \times 40 \mu\text{m}$  AFM images; (a) AFM image of 550\_300, (b) AFM image of 600\_060, (c) 2D FFT of AFM image of 550\_300 and (d) 2D FFT of AFM image of 600\_060.

## 5. Conclusion

An in-depth study was carried out on the mechanisms that affect aluminum induced texturing of soda-lime glass. It was observed that the final texture is closely related to the redox reaction products and the phases in which the process occurs. As such, the annealing temperature plays a crucial role by governing the dissolution of the reduced Si in Al and its subsequent precipitation. Most favorable surface texture was obtained below the Al-Si eutectic temperature, where the redox reaction occurred in solid phase only, leading to a controlled texturing process with uniform distribution of micro-craters.

## Acknowledgments

The authors thank The Ministry of Industry and Technology of Turkey for the financial support, Assoc. Prof. Dr. Alpan Bek and Kurtuluş Abak for the useful discussion.